Chemical
Science

ROYAL SOCIETY
OF CHEMISTRY

EDGE ARTICLE

View Article Online
View Journal | View Issue

Cite this: *Chem. Sci.*, 2026, **17**, 7729

All publication charges for this article have been paid for by the Royal Society of Chemistry

Polarizability-enhanced ionic transport in rare-earth-free halide–sulfide electrolytes: $Li_2ZrSCl_{4-x}Br_x$

Thilina N. D. D. Gamaralalage,†[a] Pawan K. Ojha, †[a] Bright O. Ogbolu, †[a] Md Mahinur Islam,[a] Tehreem Toheed,[a] Sean C. Wilkerson [a] and Yan-Yan Hu *[ab]

Received 12th November 2025
Accepted 13th February 2026

DOI: 10.1039/d5sc08802j

rsc.li/chemical-science

Commercially viable all-solid-state batteries (ASSBs) rely on solid electrolytes (SEs) that combine high ionic conductivity, electrochemical stability, low cost, and scalable production. Here, we report a series of rare-earth-free solid electrolytes, $Li_2ZrSCl_{4-x}Br_x$ ($0 \le x \le 4$), synthesized *via* a rapid, energy-efficient mechanochemical route. The optimized composition, $Li_2ZrSCl_{1.3}Br_{2.7}$, exhibits an ionic conductivity of ~1.03 mS cm^{-1}, one order of magnitude higher than Li_2ZrCl_6. Structural and morphological analyses using XRD, SEM/EDS, and ^6Li MAS NMR reveal that progressive Br^- substitution drives structural disorder, enhances anion polarizability, and yields dynamically disordered Li^+ environments conducive to rapid ion migration. Compared to the semi-crystalline Li_2ZrSCl_4 and fully brominated Li_2ZrSBr_4 end members, $Li_2ZrSCl_{1.3}Br_{2.7}$ achieves an optimal structural disorder and Li^+ ion mobility, resulting in enhanced ionic conductivity. When used as a catholyte in an ASSB with TiS_2 as the cathode active material, $Li_2ZrSCl_{1.3}Br_{2.7}$ exhibits good rate capability and stable long-term cycling performance. This work highlights the viability of $Li_2ZrSCl_{4-x}Br_x$ as a high-performance and inexpensive solid electrolyte, combining fast Li^+-ion transport, electrochemical stability, and scalable synthesis, making it a promising candidate for commercial ASSBs.

Introduction

The advancement of solid-state batteries (SSBs) hinges on developing solid electrolytes (SEs) that combine high ionic conductivity, broad electrochemical stability, and cost-effectiveness.[1,2] Traditional liquid electrolytes face inherent drawbacks such as flammability, leakage, and limited electrochemical stability, which hinder the advancement of safer and more efficient batteries.[3,4] Halides are a promising class of SEs for the next-generation ASSBs because of their compatibility with high-voltage cathode materials.[5,6] Despite the advantages of halide SEs, achieving high Li^+-ion conductivities-up to $\sim 10^{-3}$ S cm^{-1} – has largely relied on the use of expensive transition and rare-earth trivalent elements, such as in materials like Li_3YCl_6, Li_3ErCl_6, Li_3HoCl_6, and Li_3InCl_6.[7–11] More recently, pentavalent cations such as Ta^{5+} and Nb^{5+} have been introduced in compounds like $LiTaOCl_4$, $LiNbOCl_4$, $NaTaOCl_4$, further expanding the compositional landscape of high-performing but costly halide SEs.[12–14] While these materials often exhibit favorable electrochemical properties, the use of rare-earth metals introduces challenges related to high cost, limited global supply, and supply-chain concentration, which can hinder large-scale manufacturing and long-term commercialization of solid-state batteries. Consequently, the development of rare-earth-free halide electrolytes based on earth-abundant elements is an important strategy for improving material sustainability and economic viability.[15] In contrast, Li_2ZrCl_6, a rare-earth-free alternative, has garnered increasing attention owing to its lower cost and encouraging electrochemical properties.[16–18] However, its room temperature ionic conductivity still falls short for practical solid-state batteries,[19,20] highlighting the need for further enhancements.

Recent efforts to enhance the performance of Zr-based halide SEs have focused on compositional and structural modifications. These approaches include cationic substitutions at the Zr^{4+} site in Li_2ZrCl_6 – for example, $Li_{2+x}Zr_{1-x}In_xCl_6$,[21] and $Li_{2.4}Zr_{0.8}Zn_{0.2}Cl_6$,[22] – which have been shown to improve moisture stability. Similarly, anionic substitutions, such as replacing Cl^- with F^- in $Li_{2.3}ZrCl_{6.1}F_{0.2}$,[23] have been employed to widen the electrochemical stability window. More recently, researchers have explored dual-anion systems that retain the beneficial features of halides, such as high polarizability and structural softness, while integrating anions like oxide or sulfide to tailor the local coordination environment and facilitate Li^+ transport.[24–26] Notably, superionic conductivities around $\sim 10^{-3}$ S cm^{-1} have been observed for $Li_3ZrCl_4O_{1.5}$,[27]

---

[a] *Department of Chemistry and Biochemistry, Florida State University, Tallahassee, FL 32306, USA. E-mail: yhu@fsu.edu*

[b] *Center of Interdisciplinary Magnetic Resonance, National High Magnetic Field Laboratory, Tallahassee, FL 32310, USA*

† These authors contributed equally.

$Li_{3.1}ZrCl_{4.9}O_{1.1}$,[28] $Li_3Zr_{0.75}OCl_4$,[29] and ZrO_2–2LiCl–Li_2ZrCl_6.[30] Additionally, Xu and co-workers reported a Li^+ conductivity of 0.86 mS cm^{-1} for $Li_{2.2}ZrCl_{5.8}S_{0.2}$.[31] However, these materials require long milling durations, LiCl precursor, and/or secondary heat treatments, posing challenges for industrial scalability. Motivated by these advancements and limitations, we sought to further expand the compositional space by developing a new series of rare-earth-free solid electrolytes, $Li_2ZrSCl_{4-x}Br_x$ ($0 \leq x \leq 4$). This system leverages a diversified anion framework and mixed halide composition, leading to improvements in ionic conductivity from scalable synthesis.

In this work, we report the synthesis of the $Li_2ZrSCl_{4-x}Br_x$ composition by directly combining Li_2S and ZrX_4 (X = Cl or Br), avoiding the commonly used LiCl precursor. This approach shortens the milling time, as pre-formed LiCl is highly crystalline and less reactive. The resulting Li_2ZrSCl_4 (LZSC), similar to recently reported S^{2-} doped Li_2ZrCl_6 (LZC),[32] exhibits crystalline characteristics, with observed $P\bar{3}m1$ and $C2/m$ phases, showing a modest conductivity improvement from ~0.1 in LZC to ~0.45 mS cm^{-1} in LZSC, accompanied by a substantial reduction in activation energy from ~0.41 to ~0.37 eV, highlighting sulfur's role in softening the anion framework and lowering the Li^+ migration barriers. Further Br^- substitution promotes amorphization and increases lattice softness through enhanced anion polarizability, yielding the optimized composition $Li_2ZrSCl_{1.3}Br_{2.7}$ (LZSCB), which reaches ~1.03 mS cm^{-1} at room temperature. While the activation energy remains nearly constant across the series (~0.36–0.37 eV), the conductivity enhancement arises from an increased pre-exponential factor associated with fast Li^+ ion dynamics, whereas the fully Br-substituted end member, Li_2ZrSBr_4 (LZSB), shows reduced conductivity. Importantly, the amorphous $Li_2ZrSCl_{1.3}Br_{2.7}$ material can be synthesized through a single-step 2-hour mechanochemical process, offering a practical and scalable route for industrial production. To gain deeper insight into the structure, composition, and surface morphology, a suite of characterization techniques – including NMR, XRD, SEM, EDS, and Raman spectroscopy – was utilized. As a catholyte in an ASSB comprising TiS_2 as cathode active material, Li_6PS_5Cl separator, and Li/In alloy anode, LZSCB demonstrates a good room-temprature cycling performance with 94% capacity retention (248 mAh g^{-1}) over 70 cycles at 0.2C. Our findings highlight LZSCB with remarkable conductivity, stability, and ease of production with low cost, positioning it for applications in commercially viable ASSB technologies.

Materials & methods

Synthesis

Lithium sulfide (99.5%, Alfa Aesar), $ZrCl_4$ (99.9%, Alfa Aesar), and $ZrBr_4$ (99.9%, Alfa Aesar) were stored in an argon-filled glovebox (VTI) with moisture and O_2 levels below 0.1 ppm. Subsequently, a stoichiometric amount of the starting precursors was manually ground for 15 min to achieve a homogeneous powder. The ground powder was subsequently loaded into a 20 mL zirconia milling jar with three 10 mm-sized zirconia balls, and vacuum sealed within the argon-filled glovebox. The sealed jar was placed in a High-Energy Ball Mill (8000 M Mixer/Mill®) and milled for 2 h. The processed sample was thereafter stored in the argon-filled glovebox for further characterization.

Scanning electron microscopy (SEM) and energy dispersive X-ray spectroscopy (EDS)

The samples were mounted on aluminum stubs using carbon tape to ensure electrical conductivity during SEM analysis. SEM imaging was conducted using a JEOL JSM-7000F microscope operated at an accelerating voltage of 15 kV. Prior to imaging, samples were sputter-coated with a thin layer of iridium to minimize charging effects. EDS analysis was performed in conjunction with SEM to determine the elemental composition of the samples. EDS spectra were collected and analyzed using an Oxford Instruments X-Max detector and Aztec software to quantify the elemental distribution across different regions of the samples. The working distance was maintained at 10 mm to optimize both imaging resolution and EDS signal detection.

Solid-state NMR

^6Li and ^7Li solid-state magic-angle-spinning (MAS) NMR spectra were acquired using a Bruker Avance III system equipped with a 500 MHz (11.74 T) ultrashield wide-bore magnet (89 mm). The Larmor frequencies were 73.6 MHz for ^6Li and 194.4 MHz for ^7Li. Samples were sealed in 2.5 mm zirconia rotors under an argon atmosphere and measured under an MAS rate of 24 kHz. Single-pulse ^6Li and ^7Li NMR experiments were performed with a $\pi/2$ pulse length of 3.3 μs and recycle delays of 200 s and 20 s, respectively. To study the ion dynamics in $Li_2ZrSCl_{4-x}Br_x$, the inversion-recovery approach was employed to measure ^7Li T_1 NMR relaxation times at variable temperatures. The T_1 experiments were performed on a 300 MHz spectrometer operating at the ^7Li Larmor frequency of ~116 MHz, with chemical shift calibration against $LiCl_{(s)}$ at −1.1 ppm. ^{35}Cl and ^{79}Br MAS NMR experiments were performed using an 800-MHz Bruker spectrometer with a field strength of 19.6*T*. The Larmor frequencies for ^{35}Cl and ^{79}Br were 208.3 MHz and 40 MHz, respectively. A single-pulse sequence was used for both ^{35}Cl and ^{79}Br experiments with a $\pi/2$ pulse length of 5.6 μs and 2.2 μs each and a recycle delay of 10 s and 5 s, respectively. Sample powders were packed under argon into 3.2 mm ZrO_2 pencil rotors and spun at 16 or 17 kHz. ^{35}Cl experiments were calibrated to a 0.1 M NaCl in D_2O solution at 0 ppm. ^{79}Br NMR experiments were calibrated to solid KBr at 54.5 ppm.

Raman spectroscopy

Raman spectra were collected on a Horiba JY LabRam HR Evolution spectrometer using a 532 nm excitation laser and a 600 g per mm grating. Spectra were acquired over the 100–1000 cm^{-1} range with a laser power of 20 mW and an integration time of 4 seconds. The resulting data were processed using LabSpec 6 software.

Electrochemical impedance spectroscopy (EIS)

The synthesized sample was hand-ground and pressed at 300 MPa in an 8 mm diameter PEEK mold to make a ∼0.8 mm thick pellet for AC impedance measurements. The pellet was assembled in a split cell with steel as the blocking electrode. The electrochemical impedance measurements were carried out using a Gamry electrochemical analyzer, spanning frequencies from 5 MHz to 1 Hz, with an applied voltage of 10 mV. Ionic conductivities were calculated from the impedance values extracted from the Nyquist plots and pellet dimensions. A CSZ Microclimate chamber was used to perform impedance measurements across a range of temperatures from −20 to 60 °C. Electronic conductivity was evaluated using DC polarization in a symmetric steel|$Li_2ZrSCl_{4-x}Br_x$|steel configuration. Steady-state currents were recorded at applied voltages of 100, 200, 300, and 400 mV.

Lab X-ray diffraction

The sample was sealed on a zero-background holder using Kapton film and analyzed using a Rigaku SmartLab X-ray diffractometer equipped with a Cu Kα radiation source ($\lambda = 0.154$ nm) in Bragg–Brentano geometry. Diffraction data were collected over a 2θ range of 10° to 70°, with a step size of 0.03° and a scan rate of 1.5° min^{-1}.

Linear sweep voltammetry (LSV) measurements

Approximately 150 mg of $Li_2ZrSCl_{4-x}Br_x$ was weighed into a 10 mm diameter polyether ether ketone (PEEK) cylinder and pressed at 250 MPa for 1 min. A composite with a mass ratio of 9 : 1 of $Li_2ZrSCl_{4-x}Br_x$ to carbon nanofiber was hand-ground in an agate mortar for 15 minutes. An 8-mg portion of this composite was spread over one side of the $Li_2ZrSCl_{4-x}Br_x$ pellet, contained in the PEEK cylinder, to serve as the working electrode, and pressed at 350 MPa for 1 minute. Indium foil (∼7.9 mm diameter) and lithium foil (∼4.8 mm diameter), both with a thickness of 0.1 mm, were hand-pressed onto the opposite side of the pellet. The cell was then placed into a stainless-steel casing with a constant pressure of 250 MPa. The LSV measurement was performed with a scan rate of 0.1 mV s^{-1} using a BioLogic SP-300.

Assembly of the all-solid-state battery

All-solid-state battery (ASSB) half-cells were assembled in custom-made 10 mm diameter stainless-steel cells, using stainless-steel plungers as current collectors. All cell preparation and handling were performed in an Ar-filled glovebox with H_2O and O_2 levels below 0.1 ppm. The composite catholyte was prepared by ball milling TiS_2 powder (Sigma-Aldrich, 99.9%) with the synthesized $Li_2ZrSCl_{4-x}Br_x$ electrolyte in a 1 : 2 weight ratio (TiS_2 : SE) for 30 min. Approximately 12 mg of the catholyte mixture was uniformly distributed onto one side of the separator pellet, corresponding to an areal capacity of approximately 1.22 mAh cm^{-2}, and compacted at 300 MPa for 10 s to ensure intimate interfacial contact. The separator consisted of a ∼100 mg Li_6PS_5Cl pellet, prepared following previously reported procedures,[33] and pressed at 300 MPa for 10 s. On the opposite side of the separator, a 7.9-mm-diameter indium foil was placed directly in contact with the pellet, followed by a 4.8-mm-diameter lithium foil (∼1 mg) to form the Li–In alloy anode *in situ*. The assembled cell was sealed with vacuum grease to prevent air exposure. Electrochemical testing was conducted at room temperature under a constant stack pressure of ∼35 MPa. Galvanostatic charge–discharge measurements were performed over a voltage window of 1.0–2.5 V *vs.* Li–In at various C-rates, where 1C was defined based on the theoretical capacity of TiS_2 (239 mAh g^{-1}).

Results & discussions

Average structure and morphology

The X-ray diffraction patterns for the as-milled $Li_2ZrSCl_{4-x}Br_x$ ($x = 0$, 2.0, 2.7, and 4.0) and Li_2ZrCl_6 reveal a clear structural evolution with increasing Br content, shown in Fig. 1a. For $x = 0$ (LZSC), the pattern indexes to a two-phase mixture comprising a trigonal $P\bar{3}m1$ polymorph and a monoclinic $C2/m$ polymorph. A transition from Li_2ZrCl_6, which typically crystallizes in the trigonal phase.[15,30] The corresponding Rietveld refinement plot, in Fig. 1b, Tables S1 and S2, confirms the coexistence of these two phases, with good agreement between the observed and calculated patterns.

The refined structural models for both polymorphs are illustrated in Fig. 1c, featuring the layered trigonal and monoclinic frameworks of LZSC and the transition toward an amorphous configuration upon partial substitution of Cl^- by the larger Br^- anion. This transition is evident in the diffraction patterns in Fig. 1a, where the Bragg peaks broaden, diminish in intensity, and shift toward lower 2θ (∼35°, 50°), consistent with lattice expansion induced by Br^- addition. At higher substitution levels ($x = 2.0$, 2.7, 4.0), as in $Li_2ZrSCl_{1.3}Br_{2.7}$, the diffraction pattern becomes increasingly featureless, with broad humps replacing sharp Bragg peaks. This behavior indicates extensive amorphization and collapse of the long-range crystalline order, Fig. 1c, while short-range structural motifs are retained. The low-intensity peak at ∼27° is likely associated with the Li_2S secondary phases.

Fig. 1d shows a scanning electron microscopy (SEM) image of the LZSCB sample (see Fig. S1 for LZSC), revealing uniform particle agglomeration and a smooth surface texture, features characteristic of an amorphous material. No evidence of crystalline domains or phase separation was observed, indicating structural homogeneity. Energy dispersive X-ray spectroscopy (EDS) mapping (also in Fig. 1d) confirmed the even distribution of constituent elements – Zr, S, Cl, and Br – throughout the sample. As expected, lithium was not detected due to EDS limitations in detecting low-atomic-number elements. To address this, nuclear magnetic resonance (NMR) was employed, offering better sensitivity for detecting and quantifying light elements such as lithium.

Local structural analysis

A comparison of the ^6Li MAS NMR spectra of LZSC and LZSCB is shown in Fig. 2a. The ^6Li MAS NMR spectrum of LZSC shows

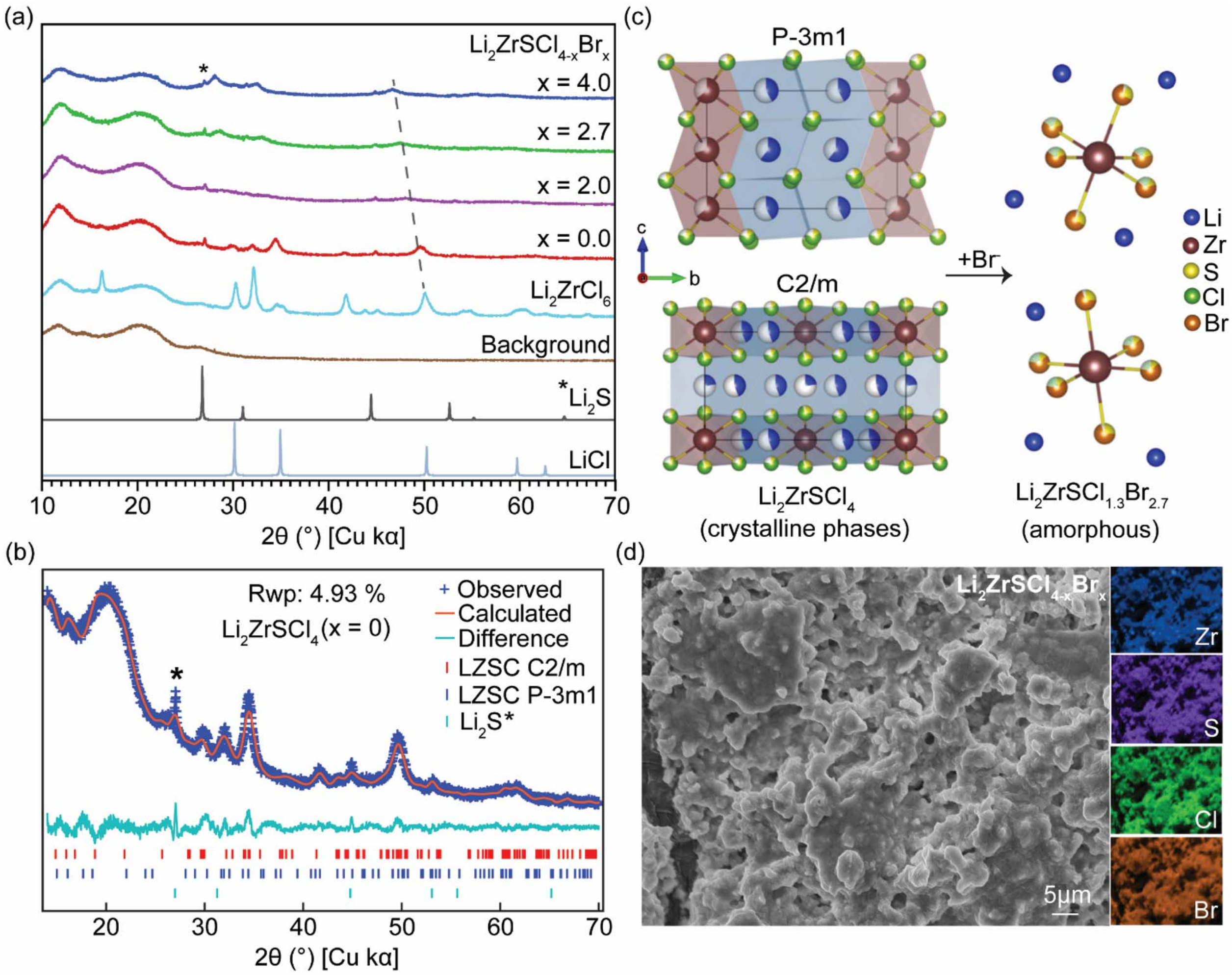

Fig. 1 Structural evolution and morphology of $Li_2ZrSCl_{4-x}Br_x$ ($0 \le x \le 4$) (a) powder X-ray diffraction of $Li_2ZrSCl_{4-x}Br_x$ showing progressive peak shifts (dashed line), peak broadening, and intensity loss with increasing Br^- content. (b) Rietveld refinement of Li_2ZrSCl_4 ($x = 0$), confirming a biphasic structure comprising trigonal $P\bar{3}m1$ and monoclinic $C2/m$ phases. (c) Crystal structure models of the $P\bar{3}m1$ and $C2/m$ polymorphs of Li_2ZrSCl_4 and schematic representation of the structural evolution upon Br^- substitution, leading to an amorphous $Li_2ZrSCl_{1.3}Br_{2.7}$ network (d) SEM micrograph and corresponding EDS elemental maps showing uniform distribution of Zr, S, Cl, and Br in $Li_2ZrSCl_{1.3}Br_{2.7}$.

two resonances at −0.68 and −0.54 ppm, consistent with the coexistence of trigonal and monoclinic phases identified by XRD (Fig. 1). The signal at −0.68 ppm (blue) likely corresponds to the more ordered trigonal phase, while the downfield resonance, −0.54 ppm, arises from Li environments in the less symmetric monoclinic lattice.

For LZSCB, only one broad isotropic resonance is observed, centered around −0.54 ppm. The line width increases from ∼19.7 Hz in LZSC to 26.9 Hz in LZSCB. The increased chemical shift dispersion with Br^- incorporation indicates increased structural disorder introduced by Br^- substitution, which broadens the range of Li-anion coordination environments and results in the wider ^{6}Li peak observed for LZSCB. This is also consistent with the extensive amorphization observed in the XRD patterns. Li_2S impurity phases are observed in both samples at ∼2.4 ppm, these could result from unreacted precursors. This residual Li_2S is also detected as a secondary impurity by XRD, evidenced by weak diffraction features. Owing to the highly disordered or partially amorphous nature of the $Li_2ZrSCl_{4-x}Br_x$ framework, quantitative phase analysis based on XRD is inherently uncertain, as peak broadening and overlap can influence refined weight fractions. ^{6}Li MAS NMR directly probes Li speciation and provides a more reliable estimate of the Li_2S content in this system. Using a long recycle delay (200 s), the integrated ^{6}Li NMR signal indicates that ∼17% of Li environments in LZSCB correspond to Li_2S, which converts to an estimated ∼2.3 wt% Li_2S[14] indicating that Li_2S is present as only a minor impurity. Similarly, a ∼3.6 wt% Li_2S is observed for LZSC. A summary of the NMR-based phase quantifications is provided in the SI (Table S3).

To better resolve the different Li sites observed in LZSC, the T_1-edited ^{7}Li MAS NMR spectrum is shown in Fig. 2b and S2, obtained from spin-lattice inversion recovery experiments at a recovery time of 0.9 s after inversion. Li^+ sites with varied ion dynamics will exhibit different T_1 relaxation behavior and thus show different recovery rates to their equilibrium states. At an intermediate relaxation time shorter than 20 s, *e.g.*, 0.9 s, the enlarged difference in intensity can help better resolve different

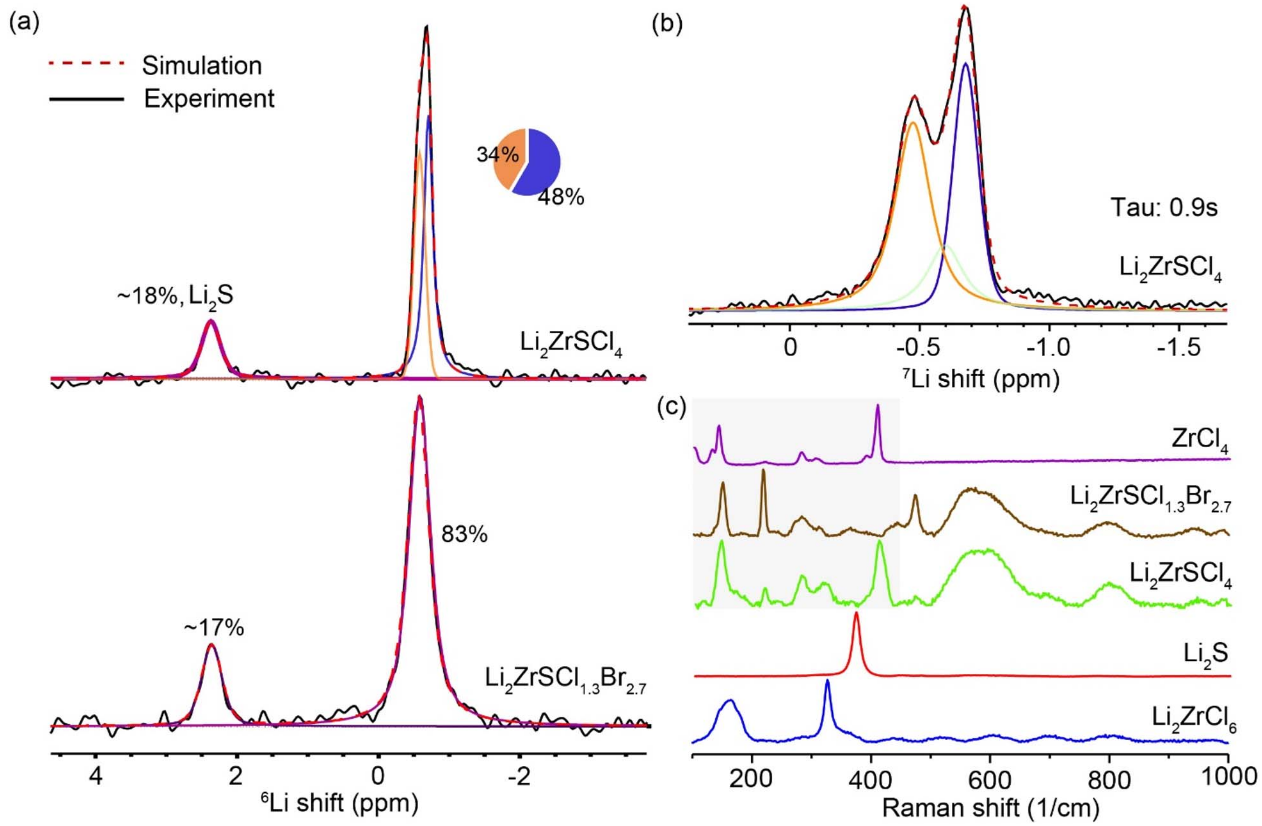

Fig. 2 Local structural environment analysis of Li^+ ions (a) ^6Li MAS NMR spectra of Li_2ZrSCl_4 and $Li_2ZrSCl_{4-x}Br_x$. (b) Select ^7Li MAS NMR spectrum obtained from inversion recovery experiments showing the different relaxation behavior of the Li sites; the full series of inversion-recovery spectra is shown in the SI, Fig. S2. (c) Raman Spectra of Li_2ZrSCl_4 and $Li_2ZrSCl_{1.3}Br_{2.7}$ compared to related structures.

components in the ^7Li NMR spectrum. Fig. 2b reveals three Li^+ sites in LZSC with slightly different T_1 relaxation times, indicating a heterogeneous local environment of Li^+ and slow exchange among these lithium sites. Whereas LZSCB shows a symmetric NMR peak, well described by a single-component fit, suggesting a more homogeneous distribution of Li sites or fast chemical exchange among different Li sites, characteristic of fast ion conductors.[34]

The Raman spectra of the $Li_2ZrSCl_{4-x}Br_x$ series, presented in Fig. 2c, confirm the presence of distorted ZrX_6 (X = Cl, Br, S) octahedra as the base structural motifs,[35] with broad, overlapping bands indicating an amorphous, disordered lattice. Compared to sharp peaks in reference compounds ($ZrCl_4$, Li_2S, Li_2ZrCl_6), the LZSC and LZSCB spectra show more peaks from the Zr–Cl/Br/S bending and stretching modes and significant broadening of these peaks due to variations in bond lengths and angles contributing to complex vibrational dynamics. The broad peaks at >500 cm^{-1} are likely to originate from Zr–S stretching vibrations in distorted or mixed-ligand octahedra such as $ZrSCl_{4-x}Br_x$. Additionally, the absence of the Li_2S peak at $\sim$370 cm^{-1} confirms sulfur incorporation into the framework.[31]

Anion substructure

Anionic local structures in $Li_2ZrSCl_{4-x}Br_x$ were directly probed using ^{35}Cl (spin-3/2) and ^{79}Br (spin-3/2) MAS NMR spectroscopy (Fig. 3). ^{35}Cl is a spin-3/2 quadrupolar nucleus, which makes its NMR behavior highly sensitive to local symmetry and electric field gradients (EFGs) around Cl^- ions. The ^{35}Cl MAS NMR of LZSC shows a sharp resonance at 9.6 ppm, suggesting a relatively symmetric local environment. The slight asymmetry is from 2nd-order quadrupolar effects. The ^{35}Cl NMR spectrum of LZSCB (Fig. 3a) exhibits an upfield shift (isotropic peak at 2.5 ppm) along with a broad (610 Hz), asymmetric lineshape, indicating increased site asymmetry and disorder from Br^- substitution in the LZSCB structure.

^{79}Br is a spin-3/2 quadrupolar nucleus, much like ^{35}Cl, but with a larger quadrupolar moment, thus more sensitive to local structural symmetry. The ^{79}Br MAS NMR spectra of $Li_2ZrSCl_{4-x}Br_x$ further reveal the impact of halide substitution on the local structure (Fig. 3b). Both LZSB and LZSCB display broad resonances on the order of several kHz, characteristic of moderate quadrupolar interactions. In LZSB, a relatively broad (4.2 kHz) isotropic peak is observed at 116 ppm, while in LZSCB, the resonance becomes even broader (8.4 kHz), suggesting a higher degree of local structural disorder and the presence of mixed halide environments.

Ion dynamics probed with T_1 NMR relaxation time measurements

To probe Li^+ dynamics in $Li_2ZrSCl_{4-x}Br_x$, ^7Li T_1 NMR relaxation times were measured across a temperature range of 25 to 85 °C

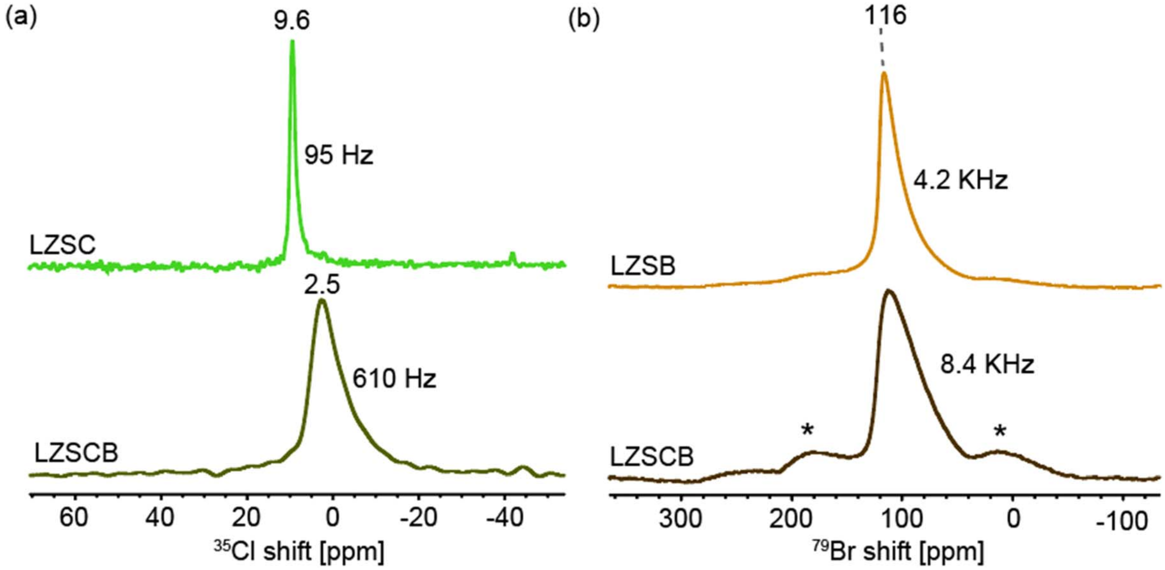

Fig. 3 Halide local environments in $Li_2ZrSCl_{4-x}Br_x$ probed with NMR (a) ^{35}Cl MAS NMR spectra of Li_2ZrSCl_4 and $Li_2ZrSCl_{1.3}B_{2.7}$ (b) ^{79}Br MAS NMR spectra of Li_2ZrSBr_4 and $Li_2ZrSCl_{1.3}B_{2.7}$.

using the inversion recovery method under static conditions, as shown in Fig. 4a. LZSC shows a relatively large T_1 across the temperature range, 1.35 s at 25 °C, indicating slower Li^+ dynamics. LZSCB, on the other hand, shows shorter T_1 values (starting at ~0.37 s at 25 °C, decreasing to ~0.15 s at 85 °C), suggesting faster Li^+ motion in the Br^- substituted material.

According to the Bloembergen–Purcell–Pound (BPP) theory[36] presented in eqn (1), T_1 is dependent on the correlation time τ_c of ionic motion.

$$\frac{1}{T_1} = \frac{3\mu_o^2\gamma^4\hbar^2}{10r_o^6}\left[\frac{\tau_c}{1+(\omega_o\tau_c)^2} + \frac{4\tau_c}{1+4(\omega_o\tau_c)^2}\right] \quad (1)$$

where $\tau_{c,}$ denotes the average residence time between consecutive Li^+ ion hops, ω_o is the Larmor frequency, γ is the magnetogyric ratio, μ_o is the magnetic permeability of free space, $\hbar$ is the reduced Planck constant, and r_o is the interatomic distance.

In the slow-motion regime, wherein $\omega_o\tau_c \gg 1$, increasing temperature leads to faster motion and shorter T_1 time due to the correlation time (τ_c) of the molecular motions approaching the Larmor frequency (ω_o). Both systems operate in the slow or intermediate motion regime, but LZSCB exhibits faster ion dynamics than LZSC, as indicated by the consistently lower T_1 values across the temperature window. Linewidth decreases with temperature in both samples (Fig. 4b), indicating dynamic averaging of dipolar interactions as lithium mobility increases.

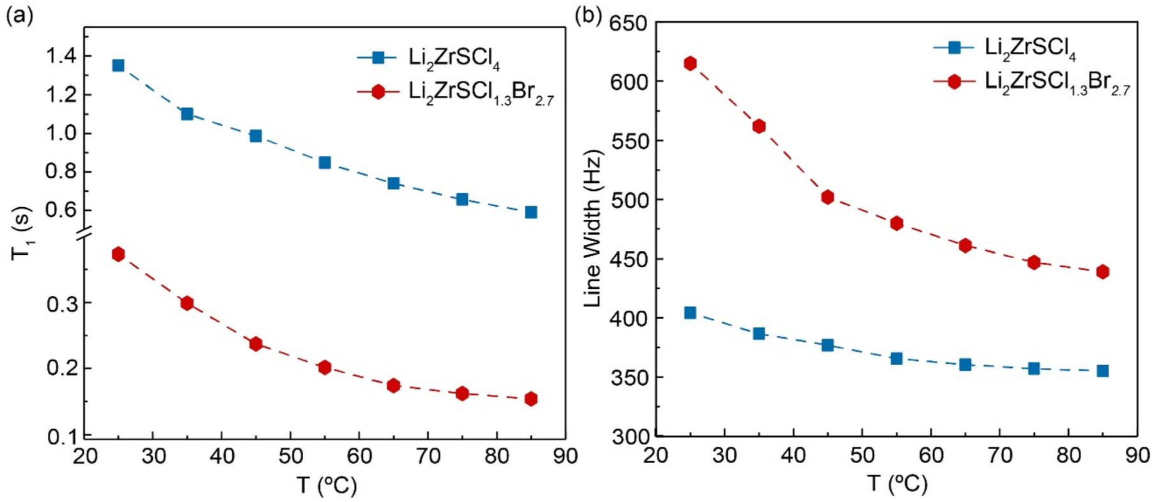

Fig. 4 (a) Variable-temperature ^7Li static T_1 relaxation times for Li_2ZrSCl_4 and $Li_2ZrSCl_{1.3}Br_{2.7}$ (b) linewidth narrowing of the ^7Li static NMR spectra with increasing temperature, due to increased motion.

LZSCB generally shows broader lines (~620 Hz at RT) compared to LZSC (~400 Hz), in agreement with increased structural disorder.

Ion transport properties determined with EIS

Fig. 5a displays the Nyquist plot and the corresponding equivalent circuit fit (inset) for the SEs at room temperature. The data were modeled using an equivalent circuit composed of two resistor–constant phase element (R||CPE) pairs in series with an additional CPE, accounting for total ionic transport and electrode interface contributions. Attempts to deconvolute bulk and grain boundary resistances, even at low temperatures (−20 °C; Fig. S3), were unsuccessful; thus, the extracted values represent total ionic conductivity.[37] Among the compositions studied, the LZSCB exhibits the highest ionic conductivity of ~1.03 mS cm^{-1}, a nearly tenfold increase compared to LZC, which shows a conductivity of 0.10 mS cm^{-1}. The intermediate composition $Li_2ZrSCl_2Br_2$ (LZSCB2) shows an intermediate ionic conductivity of ~0.57 mS cm^{-1}, while the end members LZSC and LZSB exhibit lower conductivities of 0.45 and 0.43 mS cm^{-1}, respectively (Fig. 5c and Table S4). To further investigate the transport behavior, variable-temperature (VT) impedance spectroscopy was performed (Fig. S3). The resulting Arrhenius plots (Fig. 5b and S4) show a linear dependence of conductivity on inverse temperature across the entire range, indicating the absence of phase transitions or thermal degradation. Activation energies extracted from the slopes of the Arrhenius plots were 0.41 eV (LZC), 0.37 eV (LZSC), 0.36 eV (LZSCB), 0.36 eV (LZSCB2), and 0.37 eV (LZSB).

LZC exhibits a relatively high activation energy (~0.41 eV) and low ionic conductivity (~0.1 mS cm^{-1}), indicating strongly hindered Li$^+$ migration. Upon sulfur incorporation, the activation energy decreases to ~0.36–0.37 eV across the $Li_2ZrSCl_{4-x}Br_x$ series, confirming that sulfur introduces a softer, more polarized anion lattice that lowers the intrinsic migration barrier. In comparison, Br$^-$ substitution has little effect on the activation energy but strongly influences ionic conductivity through changes in the pre-exponential factor, which increases systematically and reaches a maximum for LZSCB (Table S4).[38] This trend indicates that the conductivity enhancement is driven primarily by increased Li$^+$ ion jumping rates. This correlates with the enhanced Li$^+$ dynamics observed in the ^{7}Li T_1 NMR measurements.

The superior performance of LZSCB relative to LZSC and LZSB arises from an optimal balance between structural disorder and anion polarizability.[39] LZSCB is largely amorphous, Li$^+$ transport is governed by short-range interactions rather than long-range order. In the more crystalline LZSC, Li$^+$ migration is partially hindered by the residual crystalline domains and stronger Li–Cl interactions, which create deeper potential wells and limited site connectivity. Partial substitution of Cl$^-$ with the larger, more polarizable Br$^-$ in LZSCB further softens the anion framework, introduces intrinsic structural frustration within the disordered matrix, and increases the local free volume, as evidenced by lattice expansion and increased disorder in XRD (Fig. 1a). These effects enhance Li$^+$ site accessibility, weaken electrostatic interactions, and likely couple to low-frequency anion motions that promote dynamic Li$^+$ hopping.[24,40–44]

In contrast, the fully Br-substituted LZSB becomes more ordered, compared with partially Br-substituted compositions, leading to decreased Li$^+$ ion dynamics. While partial Br substitution enhances ionic transport relative to the Cl-rich end member, the $x = 2$ composition (LZSCB2) does not reach the maximum conductivity, demonstrating that compositional tuning beyond simple Br addition is required to achieve optimal transport behavior. Accordingly, LZSCB ($x = 2.7$) achieves superior Li$^+$ transport by inducing optimal structural disorder.[39,45,46]

The pressure dependence of ionic conductivity was evaluated under varying stack pressures, as shown in Fig. S5. Ionic conductivity increases with applied pressure due to improved particle–particle contact and reduced interfacial resistance,[47] and then plateaus at ~1.02 mS cm^{-1} between 35 and 40 MPa, with no further enhancement at higher pressures. Furthermore, electronic conductivity measurements (Fig. 5d, S6 and S7) show very low values (~10^{-9}–10^{-10} S cm^{-1}) across the $Li_2ZrSCl_{4-x}Br_x$ series, confirming that the total measured conductivity is dominated by ionic transport. Notably, Li_2S is a poor Li$^+$ conductor at room temperature[48] and, given its low volume fraction, has a negligible influence on ionic conductivity, which is dominated by the $Li_2ZrSCl_{4-x}Br_x$ framework.

Electrochemical stability and half-cell cycling

The electrochemical stability window (ESW) of the compounds was assessed using linear sweep voltammetry (LSV), shown in Fig. S8. In the Li–In|SE|SE–C setup used for this measurement, the solid electrolyte ($Li_2ZrSCl_{4-x}Br_x$) was positioned between a Li–In alloy anode and a composite cathode consisting of carbon and the SE. Li–In alloy was used as the working electrode in the LSV measurements to minimize interfacial instability and enable a reliable assessment of the electrolyte's intrinsic electrochemical stability. Compared to pure Li metal, Li–In forms a less reactive interface with solid electrolytes, suppressing parasitic reactions and interphase growth that can otherwise dominate the LSV response.[49] The LSV results reveal that Li_2ZrSCl_4 exhibits the widest electrochemical stability window (~0.7–2.6 V), due to the high oxidative stability of Cl$^-$. Partial Br substitution in $Li_2ZrSCl_{1.3}Br_{2.7}$ slightly narrows the window to ~1–2.6 V, with oxidative decomposition onset occurring near 2.6 V. Fully substituted Li_2ZrSBr_4 displays the narrowest range (~1.3–2.0 V), with both earlier oxidation and reduction, indicating it is the least electrochemically stable. Fig. S8d summarizes this trend, where the broader voltage window of the all-Cl compound aligns with the fact that Br$^-$ is more readily oxidized than Cl$^-$.[50]

When integrated into composite cathodes to facilitate ion transport, $Li_2ZrSCl_{4-x}Br_x$ SEs demonstrated excellent cycling performance in ASSB half-cells. These cells were assembled using a TiS_2:$2Li_2ZrSCl_{4-x}Br_x$ composite cathode, a Li–In alloy anode, and a Li_6PS_5Cl separator. Prior to full-cell testing, the compatibility between LZSCB and a Li metal anode was

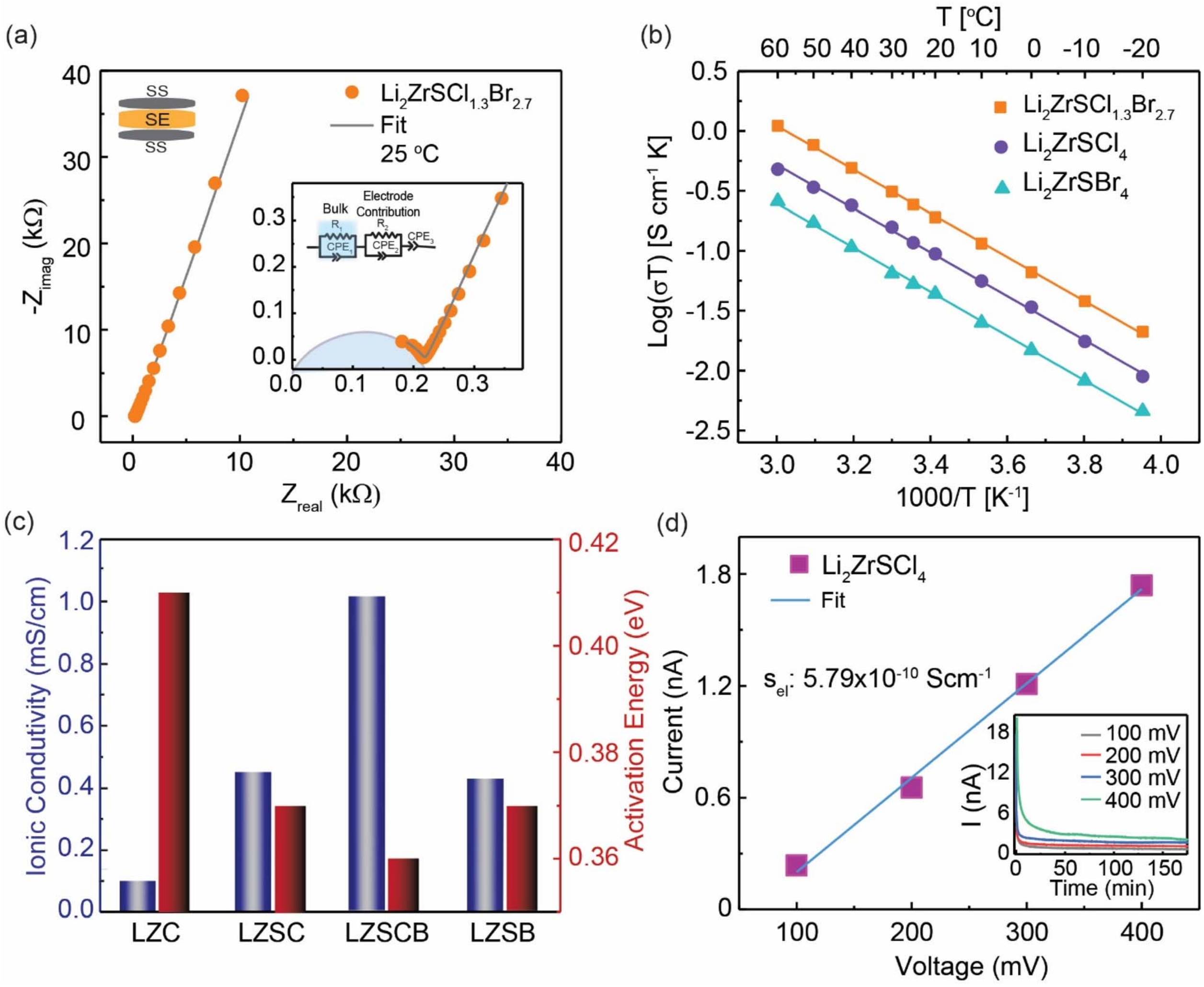

Fig. 5 Charge transport properties of $Li_2ZrSCl_{4-x}Br_x$ ($0 \leq x \leq 4$) determined with AC electrochemical impedance spectroscopy and DC polarizations. (a) Representative Nyquist plot and corresponding equivalent circuit fitting at 25 °C for $Li_2ZrSCl_{1.3}Br_{2.7}$ (b) Arrhenius-type plot for the series (c) chart showing the comparative ionic conductivity and activation energy for Li_2ZrCl_6 and $Li_2ZrSCl_{4-x}Br_x$ (d) plots from DC polarization measurements to determine the electronic conductivity.

evaluated using time-resolved impedance spectroscopy on a Li|LZSCB|Li symmetric cell (see Fig. S9). The continuous increase in interfacial impedance observed in the Li|LZSCB|Li symmetric cell indicates the non-self-limiting formation of a resistive interphase at the Li/electrolyte interface, consistent with reductive decomposition of the halide framework under direct contact with Li metal. Similar behavior has been reported for a broad range of halide solid electrolytes and reflects their limited intrinsic stability against Li.[51] In this work, Li_6PS_5Cl was intentionally used as a separator to decouple cathode performance from known interfacial challenges arising from direct contact between halide electrolytes and Li metal. This cell configuration allows LZSCB to be evaluated specifically as a catholyte, focusing on its ionic transport and compatibility within composite cathodes. Also, preliminary cycling experiments with NMC and $LiFePO_4$ (LFP) composite cathodes resulted in rapid cell failure (see Fig. S10) due to electrolyte instability at higher voltages, further supporting the selection of TiS_2 as an appropriate cathode active material for evaluating the LZSCB electrolyte system.

As shown in the voltage profiles (Fig. 6a, b and S11), at a current rate of 0.1C, initial discharge capacities reached 415 mAh g^{-1} for LZSC, 382 mAh g^{-1} for LZSCB, and 330 mAh g^{-1} for LZSB. These discharge capacities at low current densities exceed the theoretical capacity of TiS_2 (239 mAh g^{-1}), a behavior commonly reported for TiS_2–sulfide–electrolyte composite cathodes when capacities are normalized to the TiS_2 mass. This excess capacity arises from interfacial and electrolyte-derived electrochemical contributions, enabled by intimate contact between TiS_2 and the solid electrolyte.[52–55] In the present work, using ball-milled TiS_2 together with a ball-milled halide catholyte ($Li_2ZrSCl_{4-x}Br_x$) increases the interfacial area and thus the capacity contributions from interfacial reactions. These contributions, often kinetically limited, are most pronounced at low C-rates and early cycles and are progressively suppressed at higher rates, where the electrochemical response becomes increasingly dominated by TiS_2 intercalation. The capacity stabilized after the second cycle, suggesting the formation of a passivating interphase that supports reversible cycling. Rate performance tests further showcased the superior behavior of LZSCB, which delivered 322, 289, 248, 200, and 133 mAh g^{-1} at 0.1, 0.2, 0.5, 1, and 2C, respectively. In comparison, LZSC delivered 323, 263, 200, 141, and 62 mAh g^{-1}, while LZSB realized 330, 304, 235, 160, 109, and 48 mAh g^{-1}, at corresponding C-rates. The higher capacities observed for the LZSCB cell are linked to its enhanced ionic conductivity and the improved utilization of the active cathode CAM material. Notably, LZSCB retained 81% of its initial capacity after 80 cycles at 0.2C (Fig. 6c), underscoring its long-term cycling stability. These improvements are likely a result of its high ionic conductivity and enhanced compatibility at the cathode–electrolyte interface. Li_2S, present as a minor impurity, is electrochemically stable within the relevant voltage window and does not adversely affect electrolyte stability.[56] Even at a high current rate of 2C, LZSCB maintained a significantly higher specific capacity (133 mAh g^{-1}) compared to LZSC (62 mAh g^{-1}) and LZSB (48 mAh g^{-1}), highlighting its potential for application in high-performance ASSBs.

To directly probe interfacial stability during long-term cycling, we measured the EIS before and after cycling (see Fig. S12 and Table S5). EIS data reveal increased bulk and interfacial resistances after cycling (R_{bulk}: 107.8 to 146.6 Ω; Interface 1: 14.9 to 24.7 Ω; Interface 2: 35.5 to 685.5 Ω). Owing to depressed arcs and overlapping time constants, assignments are made based on frequency position and literature precedent.[57–59] The mid-frequency response (Interface 1) is

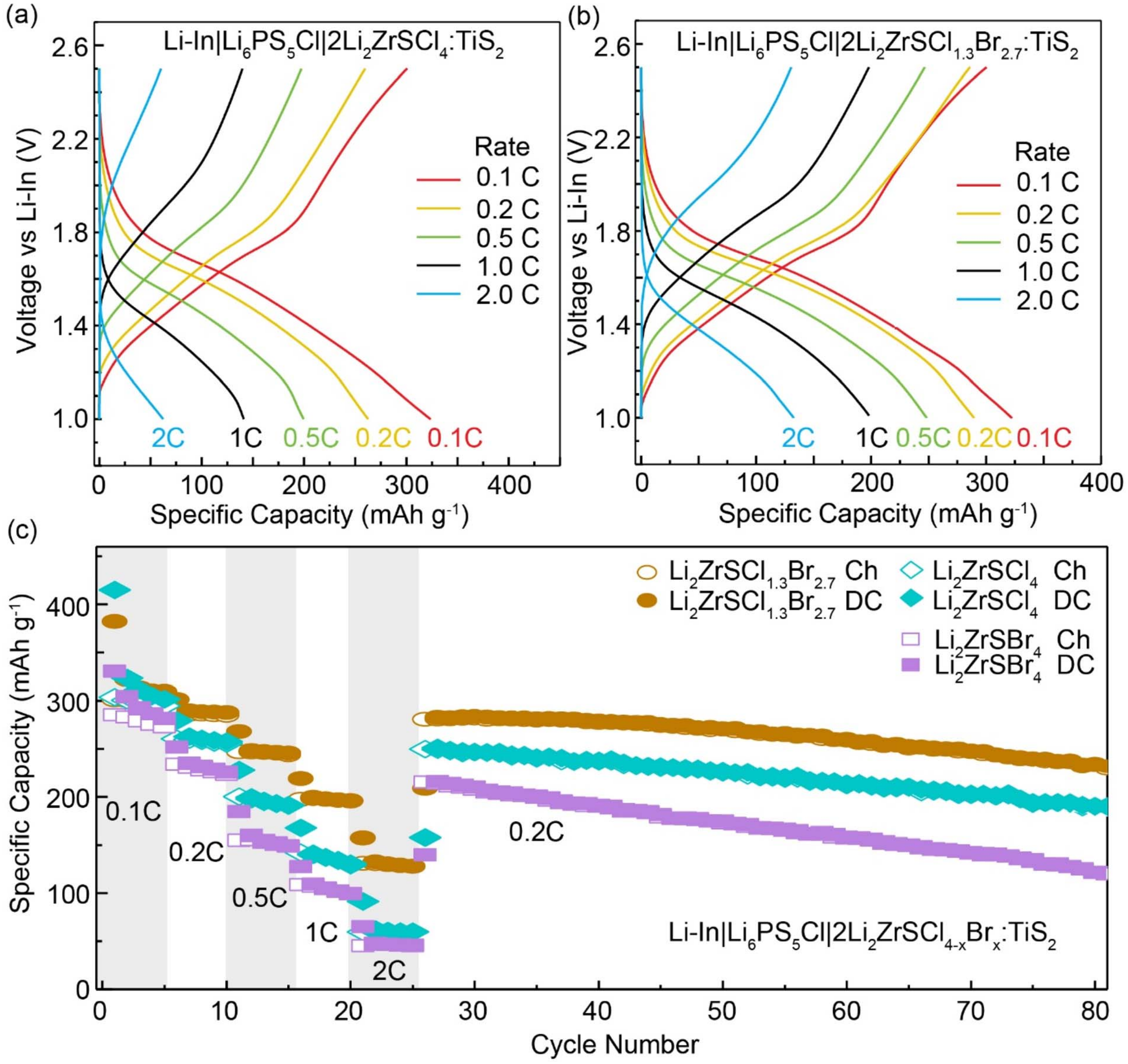

Fig. 6 Electrochemical profiles of half cells using (a) Li_2ZrSCl_4 and (b) $Li_2ZrSCl_{1.3}Br_{2.7}$ in the composite cathodes at 0.1C, 0.2C, 0.5C, 1C, and 2C, respectively. (c) The corresponding rate performance and long-term cycling stability cycled at 0.2C, where C = 239 mAh g^{-1} referenced to the theoretical capacity of TiS_2. Li_2ZrSBr_4 is included for comparison.

attributed to the TiS_2/catholyte|Li_6PS_5Cl interface and the low-frequency response (Interface 2) to the Li–In|Li_6PS_5Cl interface. The pronounced growth of the low-frequency resistance is consistent with progressive anode-side interphase formation, where sulfide electrolytes are known to form Li_2S-, Li_3P-, and LiCl-rich reduction products,[60] whereas cathode-side interphases typically involve sulfur- and phosphorus-rich species like S, polysulfides,[55,61] or in our case Li–Ti–P–S–Br–Cl phases. Despite this interfacial evolution, the cell maintains high coulombic efficiency and good capacity retention, indicating that the formed interphases are largely passivating rather than performance-limiting.

Conclusion

In this study, we developed a family of rare-earth-free halide–sulfide solid electrolytes, $Li_2ZrSCl_{4-x}Br_x$ $(0 \le x \le 4)$, synthesized *via* a rapid, energy-efficient, two-hour mechanochemical method using a mixed-anion design strategy. Structural analysis from XRD and NMR data reveals that partial Br^- substitution in Li_2ZrSCl_4 induces progressive amorphization, enhanced anion polarizability, and dynamic local disorder, leading to significantly improved Li^+ transport. The optimized composition, amorphous $Li_2ZrSCl_{1.3}Br_{2.7}$, exhibited a high ionic conductivity of 1.03 mS cm^{-1}, outperforming its end members and an order of magnitude higher than that of crystalline Li_2ZrCl_6 compound. Sulfur incorporation introduces a softer, more polarizable anion lattice that lowers the intrinsic Li^+ migration barrier from ~0.41 eV in Li_2ZrCl_6 to ~0.36–0.37 eV in $Li_2ZrSCl_{4-x}Br_x$. Whereas Br^- substitution further enhances lattice softness and promotes increased amorphization and dynamic disorder, the resulting conductivity enhancement is governed primarily by an increased pre-exponential factor, which peaks for $Li_2ZrSCl_{1.3}Br_{2.7}$, indicating optimal structural disorder that promotes fast Li^+ ion dynamics. When applied as a catholyte in all-solid-state battery half-cells, LZSCB enabled high capacities, excellent rate capability, and stable long-term cycling, retaining 81% capacity after 80 cycles at 0.2C. The good performance of the solid-state battery cells employing $Li_2ZrSCl_{1.3}Br_{2.7}$, especially at high rates, is attributed to improved ionic conductivity and favorable interfacial compatibility between cathode and solid electrolyte. These findings demonstrate that compositional tuning *via* mixed halides is an effective strategy to develop scalable, high-performance chalcohalide electrolytes for next-generation solid-state batteries.

Author contributions

Thilina N. D. D. Gamaralalage: data curation, formal analysis, investigation, validation, visualization, writing – review & editing. Pawan K. Ojha: data curation, formal analysis, investigation, validation, visualization. Bright O. Ogbolu: data curation, formal analysis, investigation, validation, visualization, writing – original draft, writing – review & editing. Md Mahinur Islam: investigation, validation. Tehreem Toheed: investigation, validation. Sean C. Wilkerson: investigation. Yan–Yan Hu: conceptualization, formal analysis, funding acquisition, project administration, resources, software, supervision, validation, writing – review & editing.

Conflicts of interest

The authors declare no conflict of interest.

Data availability

The data supporting this article have been included as part of the Supplementary information (SI). Supplementary information is available. See DOI: https://doi.org/10.1039/d5sc08802j.

Acknowledgements

The authors gratefully acknowledge support from the National Science Foundation under grant no. DMR-1847038. Solid-state NMR measurements were conducted at the National High Magnetic Field Laboratory, supported by NSF Cooperative Agreement no. DMR-1644779 and DMR-2128556 and the State of Florida. Raman spectroscopy was carried out at the Materials Characterization Laboratory, Department of Chemistry and Biochemistry, Florida State University (FSU075000MAC), with technical assistance from Dr J. S. Raaj Vellore Winfred.

References

1 Q. Wang, Y. Zhou, X. Wang, H. Guo, S. Gong, Z. Yao, F. Wu, J. Wang, S. Ganapathy, X. Bai, B. Li, C. Zhao, J. Janek and M. Wagemaker, Designing Lithium Halide Solid Electrolytes, *Nat. Commun.*, 2024, **15**(1), 1050, DOI: 10.1038/s41467-024-45258-3.

2 L. Hu, J. Wang, K. Wang, Z. Gu, Z. Xi, H. Li, F. Chen, Y. Wang, Z. Li and C. Ma, A Cost-Effective, Ionically Conductive and Compressible Oxychloride Solid-State Electrolyte for Stable All-Solid-State Lithium-Based Batteries, *Nat. Commun.*, 2023, **14**(1), 3807, DOI: 10.1038/s41467-023-39522-1.

3 S. Zhang, F. Zhao, J. Chen, J. Fu, J. Luo, S. H. Alahakoon, L. Y. Chang, R. Feng, M. Shakouri, J. Liang, Y. Zhao, X. Li, L. He, Y. Huang, T. K. Sham and X. Sun, A Family of Oxychloride Amorphous Solid Electrolytes for Long-Cycling All-Solid-State Lithium Batteries, *Nat. Commun.*, 2023, **14**(1), 3780, DOI: 10.1038/s41467-023-39197-8.

4 J. Janek and W. G. Zeier, A Solid Future for Battery Development, *Nat. Energy*, 2016, (1), 16141, DOI: 10.1038/nenergy.2016.141.

5 K. Kim, D. Park, H. G. Jung, K. Y. Chung, J. H. Shim, B. C. Wood and S. Yu, Material Design Strategy for Halide Solid Electrolytes Li3MX6(X = Cl, Br, and I) for All-Solid-State High-Voltage Li-Ion Batteries, *Chem. Mater.*, 2021, **33**(10), 3669–3677, DOI: 10.1021/acs.chemmater.1c00555.

6 K. H. Park, S. Y. Kim, M. Jung, S. B. Lee, M. J. Kim, I. J. Yang, J. H. Hwang, W. Cho, G. Chen, K. S. Kim and J. Yu, Anion Engineering for Stabilizing Li Interstitial Sites in Halide Solid Electrolytes for All-Solid-State Li Batteries, *ACS Appl. Mater. Interfaces*, 2023, **15**(50), 58367–58376, DOI: 10.1021/acsami.3c13002.

7 R. Schlem, A. Banik, S. Ohno, E. Suard and W. G. Zeier, Insights into the Lithium Sub-Structure of Superionic Conductors Li3YCl6and Li3YBr6, *Chem. Mater.*, 2021, **33**(1), 327–337, DOI: 10.1021/acs.chemmater.0c04352.

8 R. Schlem, S. Muy, N. Prinz, A. Banik, Y. Shao-Horn, M. Zobel and W. G. Zeier, Mechanochemical Synthesis: A Tool to Tune Cation Site Disorder and Ionic Transport Properties of Li3MCl6 (M = Y, Er) Superionic Conductors, *Adv. Energy Mater.*, 2020, **10**(6), 1903719, DOI: 10.1002/aenm.201903719.

9 E. Kim and Y. Kim, Investigation of the Effect of Point Defects on the Li-Ion Conductivity of Li3InCl6, *Dalton Trans.*, 2022, **51**(47), 18159–18168, DOI: 10.1039/d2dt02943j.

10 X. Li, J. Liang, J. Luo, M. Norouzi Banis, C. Wang, W. Li, S. Deng, C. Yu, F. Zhao, Y. Hu, T. K. Sham, L. Zhang, S. Zhao, S. Lu, H. Huang, R. Li, K. R. Adair and X. Sun, Air-Stable Li3InCl6 Electrolyte with High Voltage Compatibility for All-Solid-State Batteries, *Energy Environ. Sci.*, 2019, **12**(9), 2665–2671, DOI: 10.1039/c9ee02311a.

11 B. O. Ogbolu, T. P. Poudel, T. N. D. D. Dikella, E. Truong, Y. Chen, D. Hou, T. Li, Y. Liu, E. Gabriel, H. Xiong, C. Huang and Y. Y. Hu, Tailoring Ion Transport in Li3-3yHo1+yCl6-XBrx via Transition-Metal Free Structural Planes and Charge Carrier Distribution, *Adv. Sci.*, 2024, **12**(7), 2409668, DOI: 10.1002/advs.202409668.

12 T. Zhao, B. Samanta, X. M. de Irujo-Labalde, G. Whang, N. Yadav, M. A. Kraft, P. Adelhelm, M. R. Hansen and W. G. Zeier, Sodium Metal Oxyhalides NaMOCl4 (M = Nb, Ta) with High Ionic Conductivities, *ACS Mater. Lett.*, 2024, **6**(8), 3683–3689, DOI: 10.1021/acsmaterialslett.4c01145.

13 Y. Tanaka, K. Ueno, K. Mizuno, K. Takeuchi, T. Asano and A. Sakai, New Oxyhalide Solid Electrolytes with High Lithium Ionic Conductivity >10 MS/Cm for All-Solid-State Batteries, *Angew. Chem., Int. Ed.*, 2023, **62**(13), 14073, DOI: 10.1002/anie.202217581.

14 L. Zhou, J. D. Bazak, C. Li and L. F. Nazar, 4 V Na Solid State Batteries Enabled by a Scalable Sodium Metal Oxyhalide Solid Electrolyte, *ACS Energy Lett.*, 2024, **9**(8), 4093–4101, DOI: 10.1021/acsenergylett.4c01855.

15 K. Wang, Q. Ren, Z. Gu, C. Duan, J. Wang, F. Zhu, Y. Fu, J. Hao, J. Zhu, L. He, C. W. Wang, Y. Lu, J. Ma and C. Ma, A Cost-Effective and Humidity-Tolerant Chloride Solid Electrolyte for Lithium Batteries, *Nat. Commun.*, 2021, **12**(1), 4410, DOI: 10.1038/s41467-021-24697-2.

16 H. Kwak, D. Han, J. Lyoo, J. Park, S. H. Jung, Y. Han, G. Kwon, H. Kim, S. T. Hong, K. W. Nam and Y. S. Jung, New Cost-Effective Halide Solid Electrolytes for All-Solid-State Batteries: Mechanochemically Prepared Fe3+-Substituted Li2ZrCl6, *Adv. Energy Mater.*, 2021, **11**(12), 2003190, DOI: 10.1002/aenm.202003190.

17 X. Luo, Y. Zhong, X. Wang, X. Xia, C. Gu and J. Tu, Ionic Conductivity Enhancement of Li2ZrCl6Halide Electrolytes via Mechanochemical Synthesis for All-Solid-State Lithium-Metal Batteries, *ACS Appl. Mater. Interfaces*, 2022, **14**(44), 49839–49846, DOI: 10.1021/acsami.2c14903.

18 H. Zhang, Z. Yu, H. Chen, Y. Zhou, X. Huang and B. Tian, Li-Richening Strategy in Li2ZrCl6 Lattice towards Enhanced Ionic Conductivity, *J. Energy Chem.*, 2023, **79**, 348–356, DOI: 10.1016/j.jechem.2023.01.008.

19 X. Liu, F. Mi and C. Sun, A Cost-Effective Ca-Doped Li2ZrCl6 Halide Solid Electrolyte for All-Solid-State Lithium Batteries, *Chem. Commun.*, 2024, **61**, 1144–1147, DOI: 10.1039/d4cc05452k.

20 P. Ganesan, M. Soans, M. A. Cambaz, R. Zimmermanns, R. Gond, S. Fuchs, Y. Hu, S. Baumgart, M. Sotoudeh, D. Stepien, H. Stein, A. Groß, D. Bresser, A. Varzi and M. Fichtner, Fluorine-Substituted Halide Solid Electrolytes with Enhanced Stability toward the Lithium Metal, *ACS Appl. Mater. Interfaces*, 2023, **15**(32), 38391–38402, DOI: 10.1021/acsami.3c03513.

21 K. Wang, Z. Gu, H. Liu, L. Hu, Y. Wu, J. Xu and C. Ma, High-Humidity-Tolerant Chloride Solid-State Electrolyte for All-Solid-State Lithium Batteries, *Adv. Sci.*, 2024, **11**(14), 2305394, DOI: 10.1002/advs.202305394.

22 P. Lei, G. Wu, H. Liu, X. Qi, M. Wu, D. Li, Y. Li, L. Gao, C. W. Nan and L. Z. Fan, Boosting Ion Conduction and Moisture Stability Through Zn2+ Substitution of Chloride Electrolytes for All-Solid-State Lithium Batteries, *Adv. Energy Mater.*, 2025, **15**(24), 2405760, DOI: 10.1002/aenm.202405760.

23 Y. Zhang, Z. Song, L. Wang, Y. Chen, Q. Yu, G. Sun, Y. Deng, W. H. Kan and W. Luo, A Li-Rich Fluorinated Lithium Zirconium Chloride Solid Electrolyte for 4.8 V-Class All-Solid-State Batteries, *Small*, 2024, **21**(2), 2407418, DOI: 10.1002/smll.202407418.

24 M. A. Kraft, S. P. Culver, M. Calderon, F. Böcher, T. Krauskopf, A. Senyshyn, C. Dietrich, A. Zevalkink, J. Janek and W. G. Zeier, Influence of Lattice Polarizability on the Ionic Conductivity in the Lithium Superionic Argyrodites Li6PS5X (X = Cl, Br, I), *J. Am. Chem. Soc.*, 2017, **139**(31), 10909–10918, DOI: 10.1021/jacs.7b06327.

25 L. Huang, K. Barker, X. Liu, Y. Jian, S. J. Skinner, M. P. Ryan and C. Huang, A Mixed-Anion Strategy for Constructing Rapid Ion-Conducting Na Solid-State Electrolyte, *Chem. Inorg. Mater.*, 2025, **6**, 100102, DOI: 10.1016/j.cinorg.2025.100102.

26 Y. Gao, S. Zhang, F. Zhao, J. Wang, J. Zhou, W. Li, S. Deng, J. Fu, X. Hao, R. Li and X. Sun, Fluorinated Superionic Oxychloride Solid Electrolytes for High-Voltage All-Solid-State Lithium Batteries, *ACS Energy Lett.*, 2024, **9**(4), 1735–1742, DOI: 10.1021/acsenergylett.3c02243.

27 S. Zhang, F. Zhao, L. Y. Chang, Y. C. Chuang, Z. Zhang, Y. Zhu, X. Hao, J. Fu, J. Chen, J. Luo, M. Li, Y. Gao, Y. Huang, T. K. Sham, M. D. Gu, Y. Zhang, G. King and X. Sun, Amorphous Oxyhalide Matters for Achieving Lithium Superionic Conduction, *J. Am. Chem. Soc.*, 2024, **146**(5), 2977–2985, DOI: 10.1021/jacs.3c07343.

28 L. Shen, J. L. Li, W. J. Kong, C. X. Bi, P. Xu, X. Y. Huang, W. Z. Huang, F. Fu, Y. C. Le, C. Z. Zhao, H. Yuan, J. Q. Huang and Q. Zhang, Anion-Engineering Toward High-Voltage-Stable Halide Superionic Conductors for All-Solid-State Lithium Batteries, *Adv. Funct. Mater.*, 2024, **34**(48), 2408571, DOI: 10.1002/adfm.202408571.

29 J. Wang, F. Chen, L. Hu and C. Ma, Alternate Crystal Structure Achieving Ionic Conductivity above 1 MS Cm −1 in Cost-Effective Zr-Based Chloride Solid Electrolytes, *Nano Lett.*, 2023, **23**(13), 6081–6087, DOI: 10.1021/acs.nanolett.3c01468.

30 H. Kwak, J.-S. Kim, D. Han, J. Seok Kim, J. Park, G. Kwon, S.-M. Bak, U. Heo, C. Park, H.-W. Lee, K.-W. Nam, D.-H. Seo and Y. Seok Jung, Boosting the Interfacial Superionic Conduction of Halide Solid Electrolytes for All-Solid-State Batteries, *Nat. Commun.*, 2023, **14**, 2459, DOI: 10.1038/s41467-023-38037-z.

31 D. Xu, J. He, Y. He, S. Wang, G. Wu, M. Li, H. Cheng, K. Yu, X. Huang and B. Tian, Amorphization of Halide Solid Electrolytes for Lithium Super-Ionic Conductivity, *J. Mater. Chem. A*, 2024, **12**, 27694–27702, DOI: 10.1039/d4ta05362a.

32 J. Hu, B. Chen, C. Shi, L. Ma, J. Sha, Z. Gao, N. Zhao and C. He, Aliovalent Sulfur-Substitution Regulated Highly Amorphous Li2ZrCl6 Solid Electrolytes for All-Solid-State Lithium Metal Batteries, *J. Energy Chem.*, 2025, **111**, 67–78, DOI: 10.1016/j.jechem.2025.07.042.

33 S. V. Patel, S. Banerjee, H. Liu, P. Wang, P. H. Chien, X. Feng, J. Liu, S. P. Ong and Y. Y. Hu, Tunable Lithium-Ion Transport in Mixed-Halide Argyrodites Li6- XPS5- XClBrx: An Unusual Compositional Space, *Chem. Mater.*, 2021, **33**(4), 1435–1443, DOI: 10.1021/acs.chemmater.0c04650.

34 M. Uitz, V. Epp, P. Bottke and M. Wilkening, Ion Dynamics in Solid Electrolytes for Lithium Batteries: Probing Jump Rates and Activation Energies through Time-Domain Li NMR, *J. Electroceram.*, 2017, **38**(2–4), 142–156, DOI: 10.1007/s10832-017-0071-4.

35 G. M. Photiadis and G. N. Papatheodorou, Vibrational Modes and Structure of Liquid and Gaseous Zirconium Tetrachloride and of Molten ZrCl4-CsCl Mixtures, *J. Chem. Soc., Dalton Trans.*, 1998, **6**, 981–989, DOI: 10.1039/a707126d.

36 N. Bloembergen, E. M. Purcell and R. V. Pound, Relaxation Effects in Nuclear Magnetic Resonance Absorption, *Phys. Rev.*, 1948, **73**, 679.

37 M. Duchardt, S. Neuberger, U. Ruschewitz, T. Krauskopf, W. G. Zeier, J. S. Auf Der Günne, S. Adams, B. Roling and S. Dehnen, Superion Conductor Na 11.1 Sn 2.1 P 0.9 Se 12 : Lowering the Activation Barrier of Na+ Conduction in Quaternary 1-4-5-6 Electrolytes, *Chem. Mater.*, 2018, **30**(12), 4134–4139, DOI: 10.1021/acs.chemmater.8b01656.

38 J. Zahnow, T. Bernges, A. Wagner, N. Bohn, J. R. Binder, W. G. Zeier, M. T. Elm and J. Janek, Impedance Analysis of NCM Cathode Materials: Electronic and Ionic Partial Conductivities and the Influence of Microstructure, *ACS Appl. Energy Mater.*, 2021, **4**(2), 1335–1345, DOI: 10.1021/acsaem.0c02606.

39 B. C. Wood, J. B. Varley, K. E. Kweon, P. Shea, A. T. Hall, A. Grieder, M. Ward, V. P. Aguirre, D. Rigling, E. Lopez Ventura, C. Stancill and N. Adelstein, Paradigms of Frustration in Superionic Solid Electrolytes, *Philos. Trans. R. Soc. London, Ser. A*, 2021, **379**, 20190467, DOI: 10.1098/rsta.2019.0467.

40 K. Hogrefe, N. Minafra, I. Hanghofer, A. Banik, W. G. Zeier and H. M. R. Wilkening, Opening Diffusion Pathways through Site Disorder: The Interplay of Local Structure and Ion Dynamics in the Solid Electrolyte Li6+ XP1-XGexS5I as Probed by Neutron Diffraction and NMR, *J. Am. Chem. Soc.*, 2022, **144**(4), 1795–1812, DOI: 10.1021/jacs.1c11571.

41 M. Gombotz and H. M. R. Wilkening, Fast Li Ion Dynamics in the Mechanosynthesized Nanostructured Form of the Solid Electrolyte Li3YBr6, *ACS Sustain. Chem. Eng.*, 2021, **9**(2), 743–755, DOI: 10.1021/acssuschemeng.0c06694.

42 T. Krauskopf, S. Muy, S. P. Culver, S. Ohno, O. Delaire, Y. Shao-Horn and W. G. Zeier, Comparing the Descriptors for Investigating the Influence of Lattice Dynamics on Ionic Transport Using the Superionic Conductor Na3PS4-XSex, *J. Am. Chem. Soc.*, 2018, **140**(43), 14464–14473, DOI: 10.1021/jacs.8b09340.

43 S. Muy, J. Voss, R. Schlem, R. Koerver, S. J. Sedlmaier, F. Maglia, P. Lamp, W. G. Zeier and Y. Shao-Horn, High-Throughput Screening of Solid-State Li-Ion Conductors Using Lattice-Dynamics Descriptors, *iScience*, 2019, **16**, 270–282, DOI: 10.1016/j.isci.2019.05.036.

44 B. O. Ogbolu, T. N. D. D. Gamaralalage, M. M. Islam, T. Toheed, J. Sariego, T. P. Poudel, B. E. Francisco and Y. Y. Hu, Li2TaS1–XOxCl5: Triple-Anion Glassy Superionic Conductors for High-Performance Solid-State Batteries, *ACS Mater. Lett.*, 2025, **7**, 4029–4036, DOI: 10.1021/acsmaterialslett.5c01054.

45 X. Li and N. A. Benedek, Enhancement of Ionic Transport in Complex Oxides through Soft Lattice Modes and Epitaxial Strain, *Chem. Mater.*, 2015, **27**(7), 2647–2652, DOI: 10.1021/acs.chemmater.5b00445.

46 Q. Zhao, W. Wang, C. Ruan, Z. Ding and Y. Ren, Low-Content Bromine Substitution Accelerates Li+Conduction in Chloride Electrolytes for All-Solid-State Batteries, *ACS Appl. Energy Mater.*, 2025, **8**(19), 14671–14678, DOI: 10.1021/acsaem.5c02440.

47 J. M. Doux, Y. Yang, D. H. S. Tan, H. Nguyen, E. A. Wu, X. Wang, A. Banerjee and Y. S. Meng, Pressure Effects on Sulfide Electrolytes for All Solid-State Batteries, *J. Mater. Chem. A*, 2020, **8**(10), 5049–5055, DOI: 10.1039/c9ta12889a.

48 Z. Lin, Z. Liu, N. J. Dudney and C. Liang, Lithium Superionic Sulfide Cathode for All-Solid Lithium-Sulfur Batteries, *ACS Nano*, 2013, **7**(3), 2829–2833, DOI: 10.1021/nn400391h.

49 A. L. Santhosha, L. Medenbach, J. R. Buchheim and P. Adelhelm, The Indium−Lithium Electrode in Solid-State Lithium-Ion Batteries: Phase Formation, Redox Potentials, and Interface Stability, *Batter. Supercaps*, 2019, **2**(6), 524–529, DOI: 10.1002/batt.201800149.

50 S. Wang, Q. Bai, A. M. Nolan, Y. Liu, S. Gong, Q. Sun and Y. Mo, Lithium Chlorides and Bromides as Promising Solid-State Chemistries for Fast Ion Conductors with Good Electrochemical Stability, *Angew. Chem., Int. Ed.*, 2019, **58**(24), 8039–8043, DOI: 10.1002/anie.201901938.

51 L. M. Riegger, R. Schlem, J. Sann, W. G. Zeier and J. Janek, Lithium-Metal Anode Instability of the Superionic Halide Solid Electrolytes and the Implications for Solid-State

Batteries, *Angew. Chem., Int. Ed.*, 2021, **60**(12), 6718–6723, DOI: 10.1002/anie.202015238.

52 R. Koerver, F. Walther, I. Aygün, J. Sann, C. Dietrich, W. G. Zeier and J. Janek, Redox-Active Cathode Interphases in Solid-State Batteries, *J. Mater. Chem. A*, 2017, **5**(43), 22750–22760, DOI: 10.1039/c7ta07641j.

53 H. Tao, M. Zhou, R. Wang, K. Wang, S. Cheng and K. Jiang, TiS2 as an Advanced Conversion Electrode for Sodium-Ion Batteries with Ultra-High Capacity and Long-Cycle Life, *Adv. Sci.*, 2018, **5**(11), 1801021, DOI: 10.1002/advs.201801021.

54 G. F. Dewald, S. Ohno, M. A. Kraft, R. Koerver, P. Till, N. M. Vargas-Barbosa, J. Janek and W. G. Zeier, Experimental Assessment of the Practical Oxidative Stability of Lithium Thiophosphate Solid Electrolytes, *Chem. Mater.*, 2019, **31**(20), 8328–8337, DOI: 10.1021/acs.chemmater.9b01550.

55 D. Y. Oh, Y. E. Choi, D. H. Kim, Y. G. Lee, B. S. Kim, J. Park, H. Sohn and Y. S. Jung, All-Solid-State Lithium-Ion Batteries with TiS2 Nanosheets and Sulphide Solid Electrolytes, *J. Mater. Chem. A*, 2016, **4**(26), 10329–10335, DOI: 10.1039/c6ta01628f.

56 Z. Zhang, Y. Shao, B. Lotsch, Y. S. Hu, H. Li, J. Janek, L. F. Nazar, C. W. Nan, J. Maier, M. Armand and L. Chen, New Horizons for Inorganic Solid State Ion Conductors, *Energy Environ. Sci.*, 2018, **11**, 1945–1976, DOI: 10.1039/c8ee01053f.

57 C. Rosenbach, F. Walther, J. Ruhl, M. Hartmann, T. A. Hendriks, S. Ohno, J. Janek and W. G. Zeier, Visualizing the Chemical Incompatibility of Halide and Sulfide-Based Electrolytes in Solid-State Batteries, *Adv. Energy Mater.*, 2023, **13**(6), 2203673, DOI: 10.1002/aenm.202203673.

58 P. Vadhva, J. Hu, M. J. Johnson, R. Stocker, M. Braglia, D. J. L. Brett and A. J. E. Rettie, Electrochemical Impedance Spectroscopy for All-Solid-State Batteries: Theory, Methods and Future Outlook, *Chemelectrochem*, 2021, **8**, 1930–1947, DOI: 10.1002/celc.202100108.

59 J. Ruhl, L. M. Riegger, M. Ghidiu and W. G. Zeier, Impact of Solvent Treatment of the Superionic Argyrodite Li6PS5Cl on Solid-State Battery Performance, *Adv. Energy Sustain. Res.*, 2021, **2**(2), 2000077, DOI: 10.1002/aesr.202000077.

60 S. Narayanan, U. Ulissi, J. S. Gibson, Y. A. Chart, R. S. Weatherup and M. Pasta, Effect of Current Density on the Solid Electrolyte Interphase Formation at the Lithium|Li6PS5Cl Interface, *Nat. Commun.*, 2022, **13**(1), 7237, DOI: 10.1038/s41467-022-34855-9.

61 Q. Li, C. Xie, X. Jiang, C. Geng, Z. Hu, H. Ge, J. Shi, L. Wang, W. Lv and Q. H. Yang, Catalytic Solder Fuses Solid-Solid Interfaces for All-Solid-State Lithium-Sulfur Batteries, *Adv. Mater.*, 2025, **37**(38), 2507308, DOI: 10.1002/adma.202507308.